

OVERVIEW OF RESULTS FROM THE STAR EXPERIMENT AT RHIC*

K. FILIMONOV FOR THE STAR COLLABORATION

*Nuclear Science Division,
Lawrence Berkeley National Laboratory,
1 Cyclotron Road, Berkeley, CA 94720, USA
E-mail: KVFilimonov@lbl.gov*

The Relativistic Heavy-Ion Collider (RHIC) provides Au+Au collisions at energies up to $\sqrt{s_{NN}}=200$ GeV. STAR experiment was designed and constructed to investigate the behavior of strongly interacting matter at high energy density. An overview of some of the recent results from the STAR collaboration is given.

1. Introduction

One of the fundamental predictions of the Quantum Chromodynamics (QCD) is the existence of a deconfined state of quarks and gluons at the energy densities above 1 GeV/fm^3 ¹. This strongly interacting medium, the Quark Gluon Plasma (QGP), may be created in the laboratory by the collision of heavy nuclei at high energy. The current experimental program at the Relativistic Heavy-Ion Collider (RHIC) is aimed at detecting the new state of matter and studying its properties.

The Relativistic Heavy-Ion Collider is located at Brookhaven National Laboratory (New York, USA). It is capable of colliding gold ions from $\sqrt{s_{NN}}=20$ to 200 GeV per nucleon pair, protons up to $\sqrt{s}=500$ GeV, and asymmetric systems like deuterons with heavy nuclei. RHIC is also the first polarized proton collider at high energies, opening new opportunities

*This work was supported by the Division of Nuclear Physics and the Division of High Energy Physics of the Office of Science of the U.S. Department of Energy, the United States National Science Foundation, the Bundesministerium für Bildung und Forschung of Germany, the Institut National de la Physique Nucléaire et de la Physique des Particules of France, the United Kingdom Engineering and Physical Sciences Research Council, Fundação de Amparo à Pesquisa do Estado de São Paulo, Brazil, the Russian Ministry of Science and Technology and the Ministry of Education of China and the National Science Foundation of China.

to study the spin structure of the proton. Diffractive processes in high electromagnetic fields can also be studied in ultra-peripheral heavy-ion collisions.

2. STAR Detector

The Solenoidal Tracker at RHIC (STAR) is one of two large detector systems constructed at RHIC². The layout of the STAR experiment is shown in Figure 1. The main detector in STAR is the world's largest Time Projection Chamber (TPC)³ measuring trajectories of charged particles at mid-rapidity ($|\eta| < 1.4$) with full azimuthal coverage. A solenoidal mag-

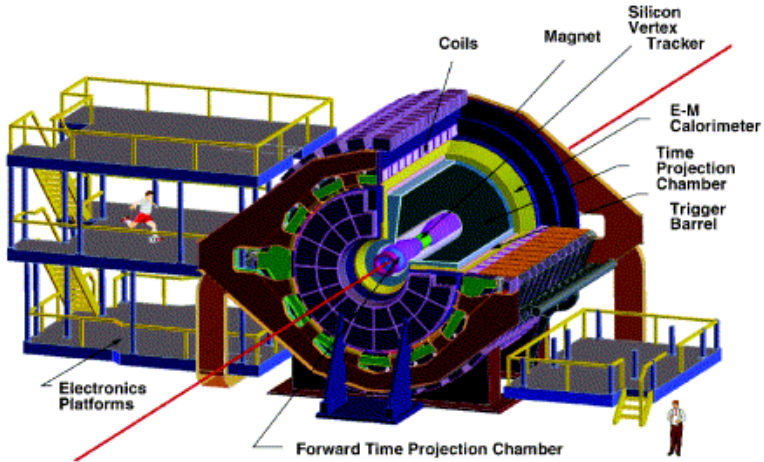


Figure 1. Schematic view of the STAR detector.

net provides a homogeneous magnetic field up to 0.5 T. Charged particle tracking close to the interaction region is accomplished by a Silicon Vertex Tracker consisting of three layers of silicon drift detectors. The high pseudorapidity range ($2.5 < |\eta| < 4$) is covered by two radial drift Forward TPCs. A barrel electromagnetic calorimeter (EMC) has been partially installed. Eventually, the full-barrel EMC and an end-cap electromagnetic calorimeter will have a combined coverage of $-1 < |\eta| < 2$. Particles are identified by their specific energy loss in the TPC gas. Particle decays in the TPC volume are identified by either their decay topology or on a statistical basis by reconstructing the invariant mass of daughter candidates.

3. Soft Physics

Relativistic heavy-ion collisions produce a large number of hadrons, most of which are in the “soft” low transverse momentum $p_T < 2$ GeV/c region of phase space. These hadrons carry important information about the collision dynamics from the early stage of the collisions to the final state interactions. The particle ratios are sensitive to the chemical properties of the system and the particle production mechanism. Measurements of the particle multiplicity, pseudorapidity, and transverse momentum distributions are valuable tools to study the bulk properties of the created system and its evolution.

3.1. *Baryon Stopping and Chemical Freeze-out*

Baryon number transport (or stopping), achieved at early stages of high-energy collisions, is an important observable sensitive to the overall dynamical evolution of the collisions. The primordial QGP to hadron phase transition a few 10^{-6} seconds after the Big Bang occurred in a nearly net-baryon free region. A dramatic increase in the antibaryon-to-baryon ratios measured at mid-rapidity is observed from SPS ($\bar{p}/p \approx 0.07$) to RHIC ($\bar{p}/p \approx 0.7$)^{4,5} energies, indicating that the system created at RHIC is getting close to net-baryon free.

STAR is particularly well-suited for studying the particle production, with results obtained for π^0 , π^- , π^+ , K^- , K^+ , K_s^0 , ρ , $K^{*0} + \overline{K^{*0}}$, f_0 , p , \bar{p} , ϕ , Λ , $\overline{\Lambda}$, Ξ^- , Ξ^+ , Ω^- , and $\overline{\Omega}^+$ ⁶. One can attempt to describe the chemical composition of the system within a thermal, chemical equilibrium model. From the experimentally measured particle ratios the chemical freeze-out parameters can be extracted. Chemical freeze-out occurs when flavor changing inelastic collisions cease. At this point the yields of various particles are fixed, and subsequent elastic scattering will not change the particle composition. Since the cross-sections for inelastic collisions are smaller than the cross-sections for elastic collisions, one expects the chemical ratios to be fixed at a time before kinetic freeze-out. Figure 2 (taken from⁷) shows the particle ratios measured at mid-rapidity for a wide variety of non-strange and strange hadrons, with the results from a statistical model fit to the data⁸. The resulting fit from this and similar models is excellent, yielding a chemical freeze-out temperature and baryon chemical potential of $T_{ch} \approx 175$ MeV and $\mu_b \approx 25 - 50$ MeV, close to the critical temperature for the deconfinement phase transition on the lattice.

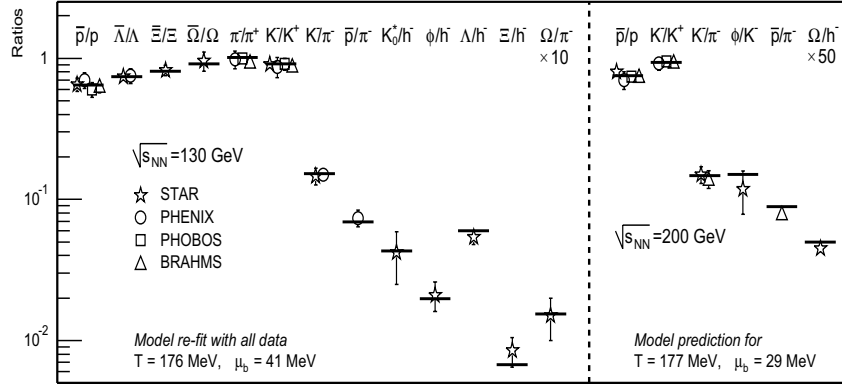


Figure 2. Particle ratios measured by the four RHIC collaborations are compared to the statistical model calculations.

3.2. Particle Spectra and Kinetic Freeze-out

Transverse momentum spectra of identified particles reflect the system properties in its final stage of thermal kinetic freeze-out, when all elastic interactions between the constituents stop. The essential parameters extracted from the data are the freeze-out temperature and velocity of the radially expanding fireball. Figure 3 shows the mid-rapidity π^- , K^- , and \bar{p} spectra for nine centrality bins in 200 GeV Au+Au collisions⁹. Systematic errors on the spectra are estimated to be 10%. The π^+ and K^+ spectra are similar to the π^- and K^- spectra, respectively. All the spectra are similar to the corresponding ones at 130 GeV^{10,11}. We fit the pion spectra with a Bose-Einstein function, the kaon spectra with a m_\perp exponential function, and the antiproton spectra with a p_\perp Gaussian function, to extract the mean transverse momenta, $\langle p_\perp \rangle$, and the dN/dy yields. The fit results are superimposed in Figure 3. The measured yields are about 65% of the extrapolated dN/dy for pions, 50-65% for kaons, and 50-75% for antiproton, respectively.

Figure 4 (left) shows the extracted $\langle p_\perp \rangle$ of π^- , K^- , and \bar{p} as a function of the mid-rapidity π^- multiplicity density, dN_{π^-}/dy , used as a measure of the collision centrality. A systematic increase with centrality is observed in the kaon and antiproton $\langle p_\perp \rangle$, consistent with collective transverse radial flow being built up in non-peripheral collisions.

Figure 4 (right) shows $\langle p_\perp \rangle$ versus particle mass for five selected systems. The p+p and most peripheral A+A results indicate no transverse radial flow; the increase in $\langle p_\perp \rangle$ with mass in these systems is due to a trivial mass

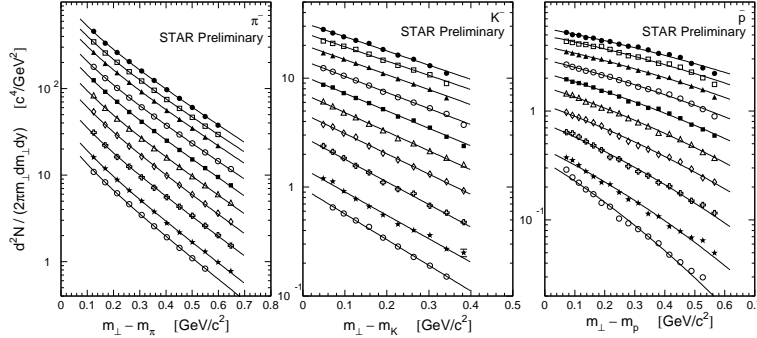


Figure 3. Preliminary mid-rapidity transverse mass spectra of π^- (left), K^- (middle), and \bar{p} (right). The lowest spectrum is from 200 GeV p+p within $|y| < 0.25$ (scaled up by a factor of 5). The other spectra are from 200 GeV Au+Au within $|y| < 0.1$, in the order of decreasing centrality from top to bottom: 5% (most central), 5-10%, 10-20%, 20-30%, 30-40%, 40-50%, 50-60%, 60-70%, and 70-80%. The pion spectra are corrected for weak decays and muon contaminations. The kaon and antiproton spectra are inclusive.

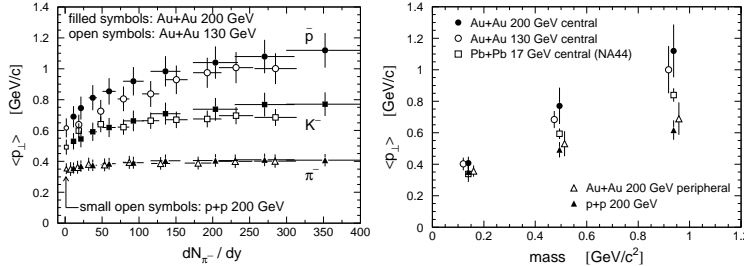


Figure 4. Left: Extracted $\langle p_\perp \rangle$ versus centrality for π^- (triangles), K^- (squares), and \bar{p} (circles) from STAR. Right: Extracted $\langle p_\perp \rangle$ versus particle mass for five collision systems.

effect. The central collision results deviate from p+p and are consistent with transverse radial flow, which appears to be stronger at RHIC than SPS.

A blast wave fit to the central π^- , K^- , and \bar{p} spectra provides a transverse radial flow velocity of $\langle \beta_T \rangle \simeq 0.55c$ at 130 GeV, and $\sim 0.60c$ at 200 GeV, with c the speed of light. The fit kinetic freezeout temperature parameters show at most a mild decrease going from SPS ($T_{\text{fo}} \simeq 110$ MeV) to RHIC ($T_{\text{fo}} \simeq 100$ MeV) energies.

4. Hard Physics

High p_T hadrons are produced in the initial collisions of incoming partons with large momentum transfer. Hard scattered partons fragment into a high energy cluster (jet) of hadrons. In elementary e^+e^- and pp collisions, jet cross sections and single particle spectra at high transverse momentum are well described over a broad range of collision energies by perturbative QCD (pQCD). Partons propagating through a dense system may interact with the surrounding medium radiating soft gluons at a rate proportional to the energy density of the medium. The measurements of radiative energy loss (jet quenching) in dense matter may provide a direct probe of the energy density¹².

4.1. High p_T : Suppression of Inclusive Spectra

Hadrons from jet fragmentation may carry a large fraction of jet momentum (leading hadrons). In the absence of nuclear medium effects, the rate of hard processes should scale with the number of binary nucleon-nucleon collisions. The yield of leading hadrons measured in Au+Au collisions at $\sqrt{s_{NN}}=130$ GeV has been shown to be significantly suppressed¹³, indicating substantial in-medium interactions. The high statistics 200 GeV data extended the measurements of hadron spectra to $p_T = 12$ GeV/c¹⁴.

Figure 5 (left) shows inclusive invariant p_T distributions of charged hadrons within $|\eta|<0.5$ for Au+Au and p+p collisions at $\sqrt{s_{NN}}=200$ GeV. The centrality-selected Au+Au spectra are shown for percentiles of σ_{geom}^{AuAu} , with 0-5% indicating the most central collisions. The measured hadron yields steeply decrease with increasing transverse momentum. Modification of inclusive spectra by nuclear effects is measured by comparison to a nucleon-nucleon (NN) reference via the nuclear modification factor:

$$R_{AA}(p_T) = \frac{d^2N^{AA}/dp_T d\eta}{T_{AA} d^2\sigma^{NN}/dp_T d\eta}, \quad (1)$$

where $T_{AA}=\langle N_{bin} \rangle / \sigma_{inel}^{NN}$ from a Glauber calculation accounts for the nuclear collision geometry. In the absence of nuclear effects, $R_{AA}(p_T)$ is expected to be unity. Figure 5 (right) shows $R_{AA}(p_T)$ at $\sqrt{s_{NN}}=200$ GeV for centrality-selected Au+Au spectra relative to the measured p+p spectrum. For $p_T < 6$ GeV/c, $R_{AA}(p_T)$ is similar to that observed at $\sqrt{s_{NN}}=130$ GeV¹³, though in the present case the NN reference and Au+Au spectra are measured at the same energy and acceptance. Hadron production for $6 < p_T < 10$ GeV/c is suppressed by a factor of 4-5 in central Au+Au relative to p+p

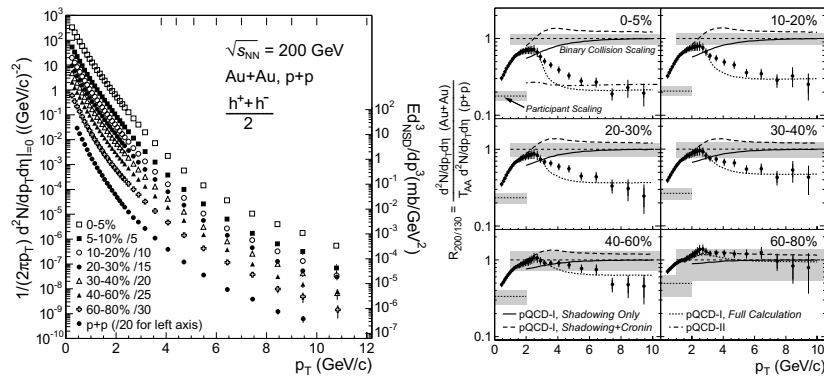


Figure 5. Left: Inclusive invariant p_T distributions of $(h^+ + h^-)/2$ for centrality-selected Au+Au and p+p non-singly diffractive interactions. Right: $R_{AA}(p_T)$ (Eq. 1) for $(h^+ + h^-)/2$ in $|\eta| < 0.5$, for centrality-selected Au+Au spectra relative to the measured p+p spectrum. The horizontal dashed lines show Glauber model expectations for scaling of the yield with mean number of binary collisions $\langle N_{\text{bin}} \rangle$ or mean number of participants $\langle N_{\text{part}} \rangle$, with the grey bands showing their respective uncertainties summed in with the p+p normalization uncertainty.

collisions. The data are compared to two calculations based on hard parton scattering evaluated via perturbative QCD (pQCD-I¹⁵ and pQCD-II¹⁶). Both pQCD models for Au+Au collisions incorporate nuclear shadowing of initial-state parton densities, the Cronin effect¹⁷, and partonic energy loss, but with different formulations. Neither pQCD calculation includes non-perturbative effects that generate particle species-dependent differences for $p_T < 5 \text{ GeV}/c$ ¹⁸. Figure 5 (right) also shows the full pQCD-I calculation and the influence of each nuclear effect. The Cronin enhancement and shadowing alone cannot account for the large suppression, which is reproduced only if partonic energy loss in dense matter is included.

4.2. High p_T : Elliptic Flow

The fragmentation products of high energy partons that have propagated through the azimuthally asymmetric system generated by non-central collisions may exhibit azimuthal anisotropy due to energy loss and the azimuthal dependence of the path length^{19,20}. The azimuthal anisotropy of final state hadrons in non-central collisions is quantified by the coefficients of the Fourier decomposition of the azimuthal particle distributions, with the second harmonic coefficient v_2 referred to as elliptic flow²¹. The elliptic

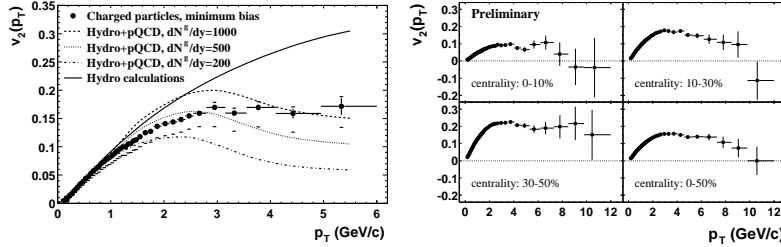


Figure 6. Elliptic flow for charged hadrons. Left panel: $v_2(p_T)$ for minimum bias at $\sqrt{s_{NN}}=130$ GeV compared to hydro and pQCD calculation. Right panel: $v_2(p_T)$ for different centralities at $\sqrt{s_{NN}}=200$ GeV.

flow measurements for $p_T < 2$ GeV/c agree in detail with hydrodynamic calculations²². Figure 6 (left panel) shows the elliptic flow v_2 as a function of p_T for Au+Au collisions at 130 GeV²³. Elliptic flow rises almost linearly with transverse momentum up to 2 GeV/c, behavior that is well described by hydrodynamic calculation. Above $p_T \sim 2$ GeV/c, $v_2(p_T)$ deviates from a linear rise and saturates for $p_T > 3$ GeV/c. The azimuthal anisotropies measured at $p_T = 4 - 6$ GeV/c are in qualitative agreement with the pQCD calculations including energy loss²⁰. Figure 6 (right panel) shows the centrality dependence of $v_2(p_T)$ measured at $\sqrt{s_{NN}}=200$ GeV²⁴. v_2 remains finite for non-central collisions, exhibiting a decrease from the saturation level at the highest measured p_T for the more central events. It is expected that the azimuthal anisotropy will vanish in the limit of very high p_T . However, at present the measured values of v_2 contain a non-flow component which at high p_T comes from intra-jet correlations. A quantitative understanding of this effect at the highest p_T especially for the most peripheral and central collisions is still needed.

4.3. High p_T : Near-angle and Back-to-Back Hadron Correlations

The large multiplicities in nuclear collisions make full jet reconstruction impractical. Correlations of high p_T hadrons in pseudorapidity and azimuth allow the identification of jets on a statistical basis. First hints of jets at RHIC came from the two-particle azimuthal distributions at $\sqrt{s_{NN}}=130$ GeV²³. Similar analysis performed for $\sqrt{s_{NN}}=200$ GeV²⁵ directly shows that hadrons at $p_T > 3 - 4$ GeV/c result from the fragmentation of jets.

Events with at least one large transverse momentum hadron ($4 < p_T^{trig} < 6$ or $3 < p_T^{trig} < 4$ GeV/c), defined to be a *trigger* particle, are used in this analysis. The trigger particles are paired with *associated* particles with $2 \text{ GeV/c} < p_T < p_T^{trig}$. An overall azimuthal pair distribution per trigger particle is then constructed:

$$D(\Delta\phi) \equiv \frac{1}{N_{\text{trigger}}} \frac{1}{\epsilon} \int d\Delta\eta N(\Delta\phi, \Delta\eta), \quad (2)$$

where N_{trigger} is the observed number of tracks satisfying the trigger requirement, and $\Delta\phi$, $\Delta\eta$ are the azimuthal and pseudo-rapidity separations between the trigger and associated particles. The efficiency ϵ for finding the associated particle is evaluated by embedding simulated tracks in real data. Figure 7 shows the azimuthal angular distribution between pairs of high p_T

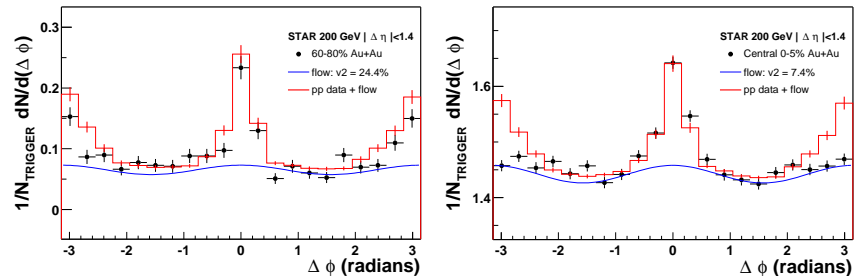


Figure 7. Azimuthal distributions of high p_T hadron pairs in Au+Au compared to p+p plus elliptic flow (STAR). Left panel: peripheral collisions. Right panel: central collisions.

hadrons for the peripheral and most central Au+Au collisions at $\sqrt{s_{\text{NN}}}=200$ GeV. The strength of near-side correlations (near $\Delta\phi = 0$) for both centralities is consistent with that measured in p+p collisions. This indicates that the same mechanism (hard parton scattering and fragmentation) is responsible for high transverse momentum particle production in p+p and Au+Au collisions. The away-side (back-to-back) correlations in peripheral Au+Au collisions may be described by an incoherent superposition of jet-like correlations measured in p+p and elliptic flow. However, back-to-back jet production is strongly suppressed in the most central Au+Au collisions. This indicates a substantial interaction as the hard-scattered partons or their fragmentation products traverse the medium. The ratio of the mea-

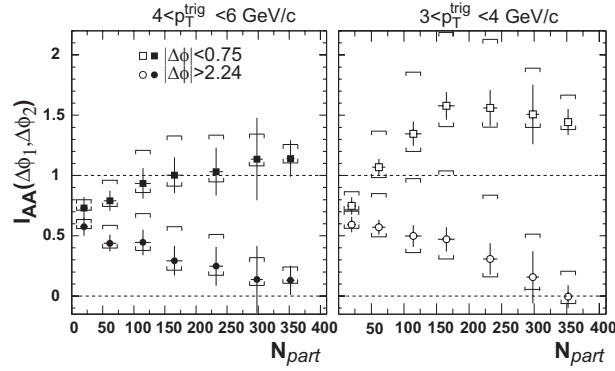


Figure 8. Ratio of Au+Au and p+p (Equation 3) for small-angle (squares, $|\Delta\phi| < 0.75$ radians) and back-to-back (circles, $|\Delta\phi| > 2.24$ radians) azimuthal regions versus number of participating nucleons for trigger particle intervals $4 < p_T^{trig} < 6$ GeV/c (solid) and $3 < p_T^{trig} < 4$ GeV/c (hollow). The horizontal bars indicate the dominant systematic error (highly correlated among points) due to the uncertainty in v_2 .

sured Au+Au correlation excess relative to the p+p correlation is:

$$I_{AA}(\Delta\phi_1, \Delta\phi_2) = \frac{\int_{\Delta\phi_1}^{\Delta\phi_2} d(\Delta\phi) [D^{AuAu} - B(1 + 2v_2^2 \cos(2\Delta\phi))]}{\int_{\Delta\phi_1}^{\Delta\phi_2} d(\Delta\phi) D^{pp}}. \quad (3)$$

The ratio can be plotted as a function of the number of participating nucleons (N_{part}). I_{AA} is measured for both the small-angle ($|\Delta\phi| < 0.75$ radians) and back-to-back ($|\Delta\phi| > 2.24$ radians) regions. The ratio should be unity if the hard-scattering component of Au+Au collisions is simply a superposition of p+p collisions unaffected by the nuclear medium. These ratios are given in Figure 8 for the trigger particle momentum ranges indicated. For the most peripheral bin (smallest N_{part}), both the small-angle and back-to-back correlation strengths are suppressed, which may be an indication of initial state nuclear effects such as shadowing of parton distributions or scattering by multiple nucleons, or may be indicative of energy loss in a dilute medium. As N_{part} increases, the small-angle correlation strength increases, with a more pronounced increase for the trigger particles with lower p_T threshold. The back-to-back correlation strength, above background from elliptic flow, decreases with increasing N_{part} and is consistent with zero for the most central collisions.

5. Summary

At RHIC, a system with low net-baryon density at mid-rapidity is produced. 2/3 of the baryons come from baryon-antibaryon pair production, while 1/3 of mid-rapidity net baryons come from the initial nuclei. The system undergoes chemical freeze-out at $T_{ch} \approx 175$ MeV and $\mu_b \approx 25 - 50$ MeV. The single particle p_T spectra suggest that the system undergoes further elastic re-scattering until final freeze-out at $\langle \beta_T \rangle \approx 0.50 - 0.6c$ and a kinetic freeze-out temperature $T_{fo} \approx 100$ MeV.

The striking phenomena that have been observed at high p_T in nuclear collisions at RHIC: strong suppression of the inclusive hadron yield in central collisions, large elliptic flow which saturates at $p_T > 3$ GeV/c, and disappearance of back-to-back jets, are all consistent with a picture in which observed hadrons at $p_T > 3 - 4$ GeV/c are fragments of hard scattered partons, and partons or their fragments are strongly scattered or absorbed in the nuclear medium. The observed hadrons therefore result preferentially from hard-scattered partons generated on the periphery of the reaction zone and heading outwards. These observations appear consistent with large energy loss in a system that is opaque to the propagation of high-momentum partons or their fragmentation products. The upcoming results from d-Au collisions at $\sqrt{s_{NN}} = 200$ GeV will help in determining whether the observed effects are due to the final state interactions.

References

1. J. W. Harris and B. Muller, Ann. Rev. Nucl. Part. Sci. **46**, 71 (1996).
2. K.H. Ackermann *et al.* [STAR Collaboration], Nucl. Instr. Methods. A **499**, 624 (2003).
3. M. Anderson *et al.*, Nucl. Instr. Methods. A **499**, 659 (2003).
4. C. Adler *et al.* [STAR Collaboration], Phys. Rev. Lett. **86**, 4778 (2001), Erratum-*ibid.* **90**, 119903 (2003).
5. C. Adler *et al.* [STAR Collaboration], Phys. Rev. Lett. **89**, 092301 (2002).
6. G. Van Buren [STAR Collaboration], Nucl. Phys. A **715**, 129c (2003).
7. T. S. Ullrich, Nucl. Phys. A **715**, 399c (2003).
8. P. Braun-Munzinger, D. Magestro, K. Redlich and J. Stachel, Phys. Lett. B **518**, 41 (2001).
9. O. Barannikova and F. Wang [STAR Collaboration], Nucl. Phys. A **715**, 458c (2003).
10. C. Adler *et al.* [STAR Collaboration], Phys. Rev. Lett. **87**, 262302 (2001).
11. C. Adler *et al.* [STAR Collaboration], arXiv:nucl-ex/0206008.
12. R. Baier, D. Schiff and B. G. Zakharov, Ann. Rev. Nucl. Part. Sci. **50**, 37 (2000).
13. C. Adler *et al.* [STAR Collaboration], Phys. Rev. Lett. **89**, 202301 (2002).

14. J. L. Klay [STAR Collaboration], Nucl. Phys. A **715**, 733c (2003).
15. X. N. Wang, nucl-th/0305010; private communication.
16. I. Vitev and M. Gyulassy, Phys. Rev. Lett. **89**, 252301 (2002).
17. D. Antreasyan *et al.* Phys. Rev. D **19**, 764 (1979); P. B. Straub *et al.*, Phys. Rev. Lett. **68**, 452 (1992).
18. I. Vitev and M. Gyulassy, Phys. Rev. C **65**, 041902 (2002).
19. X. N. Wang, Phys. Rev. C **63**, 054902 (2001).
20. M. Gyulassy, I. Vitev and X. N. Wang, Phys. Rev. Lett. **86**, 2537 (2001).
21. S. Voloshin and Y. Zhang, Z. Phys. C **70**, 665 (1996).
22. K. H. Ackermann *et al.* [STAR Collaboration], Phys. Rev. Lett. **86**, 402 (2001).
23. C. Adler *et al.* [STAR Collaboration], Phys. Rev. Lett. **90**, 032301 (2003).
24. K. Filimonov [STAR Collaboration], Nucl. Phys. A **715**, 737c (2003).
25. C. Adler *et al.* [STAR Collaboration], Phys. Rev. Lett. **90**, 082302 (2003).